PCCP

ROYAL SOCIETY OF CHEMISTRY

PAPER

Published on 19 August 2026
Licensed under CC-BY-NC 4.0

Check for updates

Cite this: *Phys. Chem. Chem. Phys.*, 2026, **28**, 21218

# The role of higher excited states in the photophysics and photochemistry of a BODIPY–phenol derivative

Marin Sapunar, [a] Ivana Antol,*[b] Vedran Brusar, [c] Mateo Forjan, [c] Prantic Debnath,[d] Marko Bogomolec, †[b] Piotr Kabacinski,[e] Goran Zgrablić, [c] Andrea Cannizzo, [d] Giulio Cerullo, [e] Nađa Došlić [a] and Silvije Vdović *[c]

Received 1st June 2026,
Accepted 27th July 2026

DOI: 10.1039/d6cp02044e

rsc.li/pccp

The photophysics and photochemistry of the BODIPY phenol derivative **1** were investigated using steady-state and time-resolved spectroscopies, combined with nonadiabatic dynamics simulations. Upon visible excitation ($\lambda > 350$ nm), rapid (sub-100 fs) internal conversion to $S_1$ leads to the characteristic BODIPY emission around 510 nm without detectable photochemistry. In contrast, UV excitation ($\lambda < 350$ nm) opens additional relaxation pathways, producing weak fluorescence in the 350–400 nm region together with photo-deamination that is presumed to occur on an ultrafast timescale. Simulations identify the high-energy emission as originating from a higher-lying charge-transfer state with phenyl-to-BODIPY (CT_PH → BP) character, where partial population trapping occurs due to restricted access to conical intersections and a relatively large interband energy gap. In contrast, photo-deamination proceeds through higher charge-transfer states with BODIPY-to-phenyl (CT_BP → PH) character and involves ultrafast C–N bond cleavage occurring before intramolecular vibrational energy redistribution. These results rationalize the excitation-wavelength-dependent photophysics and photochemistry of BODIPY–phenol derivatives and provide guidelines for future modifications.

## Introduction

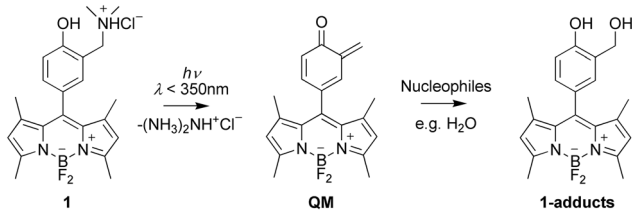
Photoluminescence processes, including fluorescence and phosphorescence, are conventionally described as originating from the lowest excited singlet or triplet state, respectively. This is generally true for photophysical processes of a majority of organic chromophores, as first formulated by M. Kasha.[1] This observation, later named Kasha's rule, can however be violated.[2,3] The most notable example is the emission from the $S_2$ state of azulene, which arises from the combination of a large energy gap between the $S_1$ and $S_2$ states, precluding fast internal conversion (IC) to the $S_1$ state, and the large oscillator strength for the $S_2 \rightarrow S_0$ transition.[4,5] Emission from $S_2$ can also occur when the $S_2$–$S_1$ energy gap is small but the $S_1 \rightarrow S_0$ transition has a low oscillator strength. In such cases, if the $S_1$ state has sufficiently long lifetime, thermal population of $S_2$ can occur, leading to observable $S_2$ emission, as in ovalene.[6,7] With the development of ultrafast optical spectroscopy,[8–10] there is increasing evidence for the emission from higher excited states, which is sometimes also called anti-Kasha fluorescence.[3] It should be noted, however, that for several molecules reported to exhibit anti-Kasha fluorescence, the assignment of emission to higher excited states has been questioned.[2]

This work focuses on the extension of Kasha's rule to photochemical reactions. Because IC between excited electronic states is typically very fast, most photochemical reactions occur from the first excited singlet or, in the case of efficient inter-system crossing, from the first triplet state.[11] However, some photoreactions have been shown to originate from higher excited states, a phenomenon often referred to as anti-Kasha photochemistry.[12] To compete effectively with IC, these reactions must proceed on ultrafast timescales.[13] Notable examples include photoinduced electron transfer (PET),[14,15] excited-state proton transfer (ESPT),[16] or photoelimination of small molecules.[17–19]

Recently, we have found that several BODIPY-phenol derivatives undergo photoelimination of an ammonium salt only

[a] *Department of Physical Chemistry, Ruđer Bošković Institute, Bijenička cesta 54, 10 000 Zagreb, Croatia*
[b] *Department of Organic Chemistry and Biochemistry, Ruđer Bošković Institute, Bijenička cesta 54, 10 000 Zagreb, Croatia. E-mail: iantol@irb.hr*
[c] *Centre for Advanced Laser Techniques, Institute of Physics, Bijenička cesta 46, 10 000 Zagreb, Croatia. E-mail: silvije@ifs.hr*
[d] *Institute of Applied Physics, Sidlerstrasse 5, CH-3012, Bern, Switzerland*
[e] *IFN-CNR, Dipartimento di Fisica, Politecnico di Milano, Piazza Leonardo da Vinci 32, I-20133 Milano, Italy*
† Current address: Department of Organic Chemistry, Faculty of Science, Charles University, Hlavova 8, 128 00 Prague 2, Czech Republic.


This journal is © the Owner Societies 2026




Scheme 1 Photoelimination of dimethylammonium from **1** that delivers **QM**.

when excited to higher excited states.[20–22] From the study by Zlatić *et al.* (ref. 20), it is known that only upon excitation of **1**, **as** shown in Scheme 1, at wavelengths shorter than 350 nm, does photoelimination of $N(CH_3)_2H^+Cl^-$ take place, delivering a quinone methide (**QM**) intermediate that subsequently reacts with nucleophilic solvents such as $H_2O$ or $CH_3OH$ to yield stable adducts (Scheme 1). The photoreactivity of **1**, which can be triggered with UV-light, and the fluorescence that is observed after visible light excitation were used for fluorescence staining of proteins.[18–20,23] However, the timescale of the photodeamination step could not be determined from previous experiments.

Owing to the excellent spectral and photophysical properties of BODIPY dyes,[24,25] their easy structural modifications,[26] and their widespread use in solar cells,[27] sensing,[28] imaging in biology[29] and phototherapy,[30] the observed deamination reaction from higher excited states may have significant potential applications. However, the mechanism of this photoreaction, which occurs only upon high-photon-energy excitation, remains unclear. In principle, excitation to a higher excited state may be required only to overcome an energy barrier for deamination on the $S_1$ surface. Here, we show that excitation to higher excited states is necessary to populate the "right" electronic state, which then drives the reaction.

By combining experiments, including steady-state and time-resolved fluorescence, fluorescence upconversion (FlUC), and femtosecond transient absorption (fs-TA), with extensive non-adiabatic dynamics simulations, we elucidate the photophysics and photochemistry of **1** and reveal the origin of the anti-Kasha behaviour observed in both fluorescence and photodeamination processes.

# Methods

## Experimental

Details on steady-state and fluorescence lifetime measurements (TC-SPC) can be found in the SI.

### Femtosecond fluorescence upconversion (FlUC)

Time resolved fluorescence is recorded by gating emission with a NIR laser in an upconversion scheme. The experimental setup follows the apparatus of N. Ernsting.[31] Pulses from an 8 kHz repetition rate amplified Ti:sapphire laser system (LIBRA, Coherent Inc.) of ~80 fs are split into two beams of 250 μJ energy. One part pumps a NIR optical parametric amplifier (OPA) to generate the gate pulse (30 μJ at 1250 nm).[32] Excitation pulses are generated by an in house visible noncollinear OPA (NOPA) and compressed with a set of chirped mirrors. The UV excitation pulses are obtained upon second harmonic generation in a β-barium borate (BBO) crystal. For the FlUC measurements, BODIPY–phenol **1** was dissolved in $CH_3CN$–$H_2O$ (1 : 1) at a concentration $c = 5.0 \times 10^{-4}$ M. An absorption spectrum before and after the FlUC measurement was recorded to monitor possible degradation of the sample. Circulation of the solution was achieved with a peristaltic pump. The fluorescence is collected in an off-axis Schwarzschild objective. Eventually, the fluorescence is gated with a type 2 frequency mixing process with the gate pulse with a suitable BBO crystal. After upconversion, the signal is coupled into a 0.7 mm single mode fiber and enters a spectrograph. The spectrum is recorded with an Andor intensified CCD camera. The data were averaged, despiked and chirp corrected. The time resolution, measured with the upconverted scattered fundamental excitation wavelength (377 nm), was 650 fs.

### fs-TA

For transient absorption experiments a homebuilt fs-TA experimental setup that was described previously was used.[33] For the measurements at wavelengths of 250, 300 and 450 nm, Orpheus–Vis optical parametric amplifier (OPA) delivering sub-50 fs pulses with a tuning range from 450 to 600 nm was used (Light Conversion, Vilnius, Lithuania). In addition, second harmonic unit extended the tuning range from 250 to 300 nm without significant change in output pulse duration. The OPA was pumped using a Pharos femtosecond laser system (Light Conversion, Vilnius, Lithuania) at 1 kHz repetition rate from which a small part of the output beam was used for the supercontinuum generation in the $CaF_2$ plate that served as a broadband probe beam covering the 340–900 nm wavelength range. For excitation at 515 nm, 0.5 mJ of the fundamental beam at 1030 nm was focused inside a hollow core fiber (Few Cycle Inc., Varennes, Canada) filled with 2.8 atm of Ar that produced stable supercontinuum supporting sub-20 fs pulses. The output was compressed and frequency doubled in 20 μm thick β BBO. Visible light pulses passed another pulse compressor after which 20 fs pulses centred at 515 nm were measured using SHG frequency resolved optical gating and used for the sample excitation. Measurements were taken by overlapping the pump and probe pulses on a 0.5 mm optical path-length spectrophotometric quartz flow cell. In experiments, the flow cell system was pumped at a rate that ensured a fresh sample volume for each pump pulse.

### Computational

Trajectory surface hopping (TSH) simulations provide detailed insight into the structural, energetic, and mechanistic aspects of ultrafast deactivation processes in small organic molecules.[34] However, applying TSH to larger systems, such as the BODIPY salt **1** studied here, remains very challenging, as compromises between the accuracy and the feasibility of the calculations are inevitable. To decrease the cost of the calculations, several

simplifications were introduced. Firstly, the chloride counterion ($Cl^-$) was disregarded and computations were performed for the solvated cation $\mathbf{1}^+$. For dynamics simulations of the cation, Tully's fewest switches surface-hopping algorithm (FSSH) was employed.[35] The ADC(2) method[36,37] with COSMO($H_2O$) solvation in conjunction with the modest def-SV(P) basis set was selected as a cost effective choice and the electronic energies as well as gradients were computed at the ADC(2)/def-SV(P) level[38] using Turbomole 7.9.[39–41] The required nonadiabatic couplings were computed from wave function overlaps.[42,43] Solvent effects were considered by water solvation as implemented in the COSMO model ($\varepsilon$ = 78.3).[44] Nonadiabatic transition probabilities were calculated by the locally diabatic version of the fewest switches surface hopping algorithm. The nuclear motion was represented by classical trajectories using a step size of 0.5 fs for a total of 1000 fs. Furthermore, since ADC(2) is not reliable in the vicinity of the $S_1/S_0$ crossing, we terminate the trajectories when the energy gap between the $S_1$ and $S_0$ states dropped below 0.1 eV.

A total of 100 initial Cartesian coordinates and velocities were sampled from a single 10 000 fs long ground state trajectory (Fig. S32) after energy equilibration at 295 K for 5000 fs. Furthermore, 20 excited state energies and ground to excited state oscillator strengths were calculated for the selected points. These data points were used for the computation of the absorption spectrum.

Furthermore, two subsets of initial conditions were selected using all calculated excitation energies and oscillator strengths. The first subset consisted of 28 trajectories with excitation energies in an energy window between 3.42 and 4.02 eV (IC1). In trajectories with initial excitation to the $S_2$, $S_3$ and $S_4$ states, the electronic energies of the 4, 5, and 6 states, respectively, were computed throughout the entire simulation.

The second subset consisted of 33 trajectories, selected within an energy window between 4.5 and 5.1 eV (IC2). In this set of trajectories, initial excitation to the $S_5$, $S_6$, $S_7$ and $S_8$ states occurred in 3, 9, 13, and 8 cases, respectively. To minimize computational cost, the number of states calculated along the trajectory was set to $N_{act}$ + 1 (where $N_{act}$ is the index of the currently populated state). This number was allowed to decrease after hops to lower excited states as long as it was greater or equal to 4. A shortcoming of the gradually decreasing number of states over the course of the trajectory, as the active state shifts to lower energies, is the inability to repopulate higher-energy states through backhopping events. This limitation will be kept in mind during the analysis of the results.

Time-dependent fluorescence spectra were obtained using the classical doorway-window scheme[45] by computing the energy gap between the active state and the ground state along with the corresponding oscillator strength at 125 fs intervals. Since the excitation pulse shape was not considered, each transition was convoluted[46] with a Gaussian function of 0.1 eV and 0.2 eV width.

The excited-state absorption (ESA) spectra of $\mathbf{1}^+$ were calculated from all trajectories (geometries) at the end of the simulation (1 ps) as vertical transitions from the current state to all higher excited states up to $S_{20}$. Each transition was convoluted with a Gaussian function of 0.2 eV width.

The TSH simulations were carried out using a development version of the ZagHop program package.[47] Molden[48] and Gabedit[49] were used for geometry manipulations and visualizations of geometries and orbitals.

# Results

### Absorption, steady-state fluorescence and time-correlated single photon counting

Fig. 1a shows the absorption spectrum of **1** in $CH_3CN$–$H_2O$ (1 : 9 v/v), while Fig. S1 displays the spectrum in $CH_3CN$–$H_2O$ (1 : 1 v/v). The two spectra are nearly identical, indicating that the ground-state electronic structure of **1** is largely insensitive to the solvent composition. Both spectra are dominated by a strong band with a maximum at 498 nm, corresponding to the $S_0 \rightarrow S_1$ transition, characteristic of the BODIPY moiety of **1**.[22,24,25] At shorter wavelengths, several weaker absorption bands are observed and are assigned based on computations (*vide infra*). The fluorescence spectrum of **1** in $CH_3CN$–$H_2O$ upon excitation in the visible range ($\lambda > 350$ nm), gives rise to a strong fluorescence emission with a maximum at 510 nm

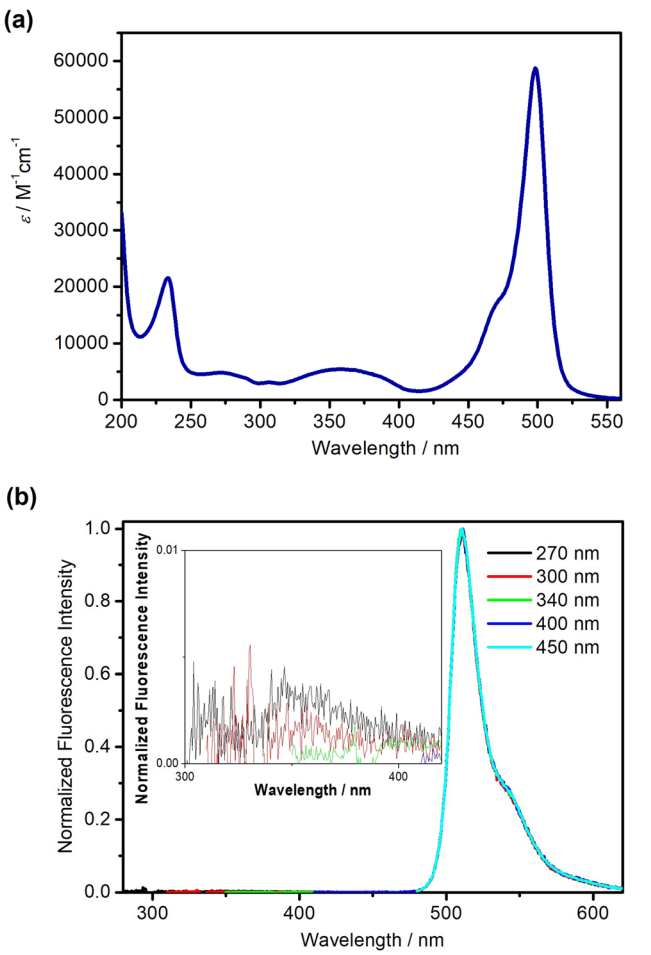



Fig. 1 (a) Absorption spectrum of **1** in $CH_3CN$–$H_2O$ (1 : 9 v/v). (b) Fluorescence spectra of **1** in $CH_3CN$–$H_2O$ (1 : 1, v/v) upon excitation at different wavelengths.


This journal is © the Owner Societies 2026

(Fig. 1b). Upon excitation in the UV ($\lambda$ < 350 nm), which initiates the photodeamination,[20] in addition to the band at 510 nm, weak emission is also detected at 350–400 nm, indicating that it originates from higher excited states (Fig. 1b).

Time-correlated single photon counting (TC-SPC) fluorescence lifetime measurements were performed by exciting at 280, 340 and 450 nm, and by detecting emission at 360 or 510 nm. The fluorescence decays (Table S1) were fit to a sum of two exponentials, with a fast decay component of <100 ps, which could not be precisely determined as it was shorter than the instrumental response function of the setup, and a longer decay component of 3.8–5.5 ns. The fluorescence kinetics at 360 nm differ from those at 510 nm under 280 nm excitation (Table S1), supporting the assignment of the 360 nm emission to a distinct, higher-lying excited state.

The 510 nm long component lifetime (3.9 ± 0.1 ns) is essentially independent of excitation wavelength across the 280–450 nm range (Table S1), consistent with emission from a common, thermalized $S_1$ minimum populated by efficient internal conversion regardless of the initially excited state. In contrast, the 360 nm long component differs in both lifetime (5.49 ns at 280 nm *vs.* 4.8 ns at 340 nm) and amplitude (84% *vs.* 8%) between the two UV excitations, supporting its assignment to a different emitting state and indicating that this state is populated through different routes (and possibly accompanied by different relaxation/quenching dynamics) at 280 *vs.* 340 nm.

### Fluorescence upconversion (FlUC)

To investigate emission from higher excited states with better time resolution, FlUC measurements were performed upon excitation with fs laser pulses at 495 nm, 335 nm and 272 nm (Fig. 2). The excitation at $\lambda$ = 495 nm shows only fluorescence from the $S_1$ state at 530 nm, which possesses both fast picosecond and slow nanosecond dynamics (Table S2). We note some minor discrepancy between the spectral position of fluorescence measured with FlUC as compared to steady state measurements, which is due to wavelength calibration. It is important to note that, for excitation at 495 nm, wavelengths shorter than 400 nm are not shown in Fig. 2a due to limitations of the detection. Although fluorescence at wavelengths shorter than the excitation wavelength is generally unlikely, processes such as two-photon absorption can excite the molecule to higher states, which then emit at wavelengths below 495 nm. On the other hand, excitation at 335 nm produces a fluorescence band centred around 370 nm, which is also observed upon excitation at 272 nm. It decays with dynamics similar to the fluorescence from the $S_1$ state, although the time constants differ (Table S2). Thus, the FlUC measurements indicate long-lived emission from higher excited states upon excitation at $\lambda$ < 350 nm.

Analysis of the fluorescence decay upon excitation at 335 nm and 272 nm reveals that the anti-Kasha fluorescence peak at 370 nm becomes narrower and exhibits a slight temporal shift toward shorter wavelengths (Fig. S11). In both cases, this shift occurs on a timescale of approximately 10 ps and is likely caused by small conformational relaxations due to the slow intramolecular rearrangements following the excitation and thermalization with the solvent.[50,51]

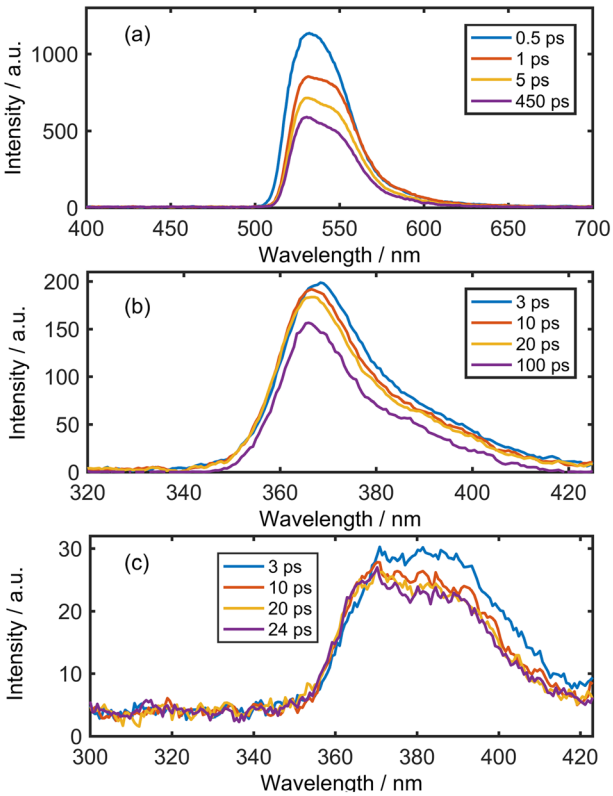



Fig. 2 FlUC spectra of BODIPY–phenol after excitation at various wavelengths. (a) $\lambda_{exc}$ = 495 nm; (b) $\lambda_{exc}$ = 335 nm; (c) $\lambda_{exc}$ = 272 nm. For the excitation in the UV, much stronger fluorescence from the $S_1$ state detected around 530 nm is not shown.

### Transient absorption measurements

Laser flash photolysis experiments on **1** upon excitation at 355 nm enabled the detection of **QM** ($\lambda_{max}$ ≈ 390 and 510 nm, $\tau$ = 2.4 ± 0.5 ms), whereas excitation of the $S_1$ at 500 nm produced negative signals due to reversible bleaching of the chromophore and stimulated emission.[20] Here, we employed femtosecond transient absorption (fs-TA) to elucidate the early photophysical processes and confirm that the photochemistry occurs from higher excited states. We aimed to determine the longest excitation wavelength at which **QM** generation takes place. The fs-TA spectral data are characterized by the overlap of the negative signals due to ground state bleaching (GSB) and stimulated emission (SE) of **1** with the positive signals due to excited state absorption (ESA) of **1** ($S_n$) and to the photoinduced absorption (PA) of the long-lived intermediate **QM**. In the following, we focus on the spectral differences and kinetics obtained at different excitation wavelengths.

Fs-TA spectra were measured upon excitation with several wavelengths from UV (250 nm) to visible (515 nm) with time-resolution of around 50–80 fs. Although we initially followed the transient response up to 900 ps (Fig. S12), we focused our

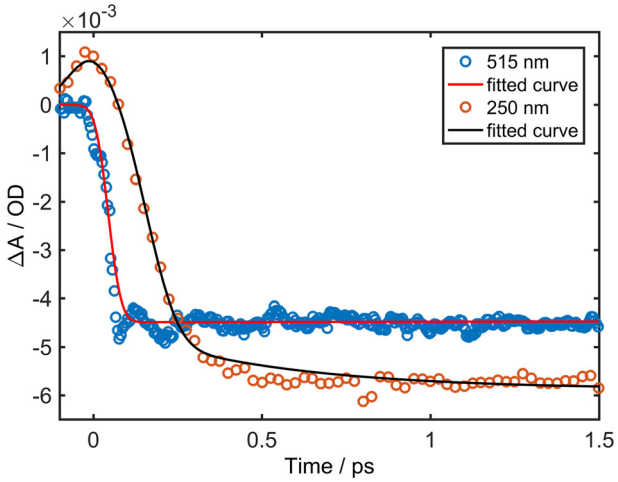



Fig. 3 Delayed rise of transient absorption at 500 nm for the excitation in the UV at 250 nm compared to the visible excitation at 515 nm.

attention on the early dynamics. Upon excitation in the visible region (515 nm), a strong negative band centred around 500 nm appeared within the time resolution of the instrument (Fig. 3 and Fig. S12). By comparing the fs-TA spectra with the absorption (Fig. 1a) and steady-state fluorescence of **1** (Fig. 1b) this band was assigned to the GSB of **1**($S_0$) and SE of **1**($S_1$). On longer time scales, GSB and SE decay with two time constants, consistent with the TC-SPC results (Table S1 and Fig. S13). At 500 nm these constants are around 100 ps and 3.6 ns. In addition to the negative signal, a positive signal was detected with two maxima centred around 350 nm and 425 nm. Again, a two exponential decay was sufficient to describe the kinetic profiles with faster time constants of 80 ps (425 nm) and 50 ps (350 nm) and a nanosecond long time constant that could not be precisely evaluated. However, it can be concluded that the dynamics of GSB and SE follow the fluorescence decay at 510 nm excited in the visible or in the UV.

It must be noted that the computed ESA of **1**($S_1$) and the absorption of **QM** ($S_0$) (*vide infra*) overlap, precluding time resolution of their formation and decay. Note also that **QM** PA was detected on much longer microsecond time scales, after the decays of GSB and SE.

We move on to the excitation wavelength dependence of fs-TA on short timescales. According to the literature,[20] excitation of **1** in $CH_3CN$–$H_2O$ (1 : 1) below 350 nm is expected to initiate deamination, whereas excitation above this threshold should lead only to non-reactive relaxation. Measurements on our TA spectrometer with sub-100 fs time resolution after UV excitation at 250 nm (Fig. 3) revealed that GSB and SE exhibit a delayed rise. Due to the significant difference in the excitation and detection wavelengths, we expect that group velocity mismatch is at least in part responsible for this effect. Based on the optical properties of the solvent used, we estimate group velocity mismatch between 250 nm and 500 nm to result in 200 fs rise time for the 0.5 mm path length. Nevertheless, the calculated deconvoluted rise time at 500 nm after excitation at 250 nm is 233 fs and we speculate that it could be evidence of a delayed rise due to population trapping in the higher excited states of **1** (*vide infra*). Details on the fitting procedure can be found in the SI.

Characteristic TA spectra and decay associated spectra (DAS) for excitation wavelengths between 250 and 515 nm are shown in Fig. S17. When excited in the UV, the shape of the short-lived DAS (~4 ps) indicates the combination of redshift with decay of the GSB + SE band between 450 and 600 nm. The corresponding short-lived DAS components for visible excitation are significantly different, showing only a minor redshift without decay within the same time window. The most plausible explanation for the initial rapid decrease in the absolute signal value within 10 ps, together with the subtle shift, observed for excitation with higher photon energy is structural change for which we speculate that it may be connected to the initiation of the chemical reaction. Cooling effects could also play a role in the observed initial picosecond decay. As the time constants of dynamical changes of FlUC and fs-TA are quite similar, we believe that they have the same origin. The long-lived DAS components, in contrast, are similar in shape across all excitation wavelengths (Fig. S17). Were **QM** contributing significantly to the TA signal on these timescales, the long-lived DAS at UV excitation would be expected to exhibit a distinct spectral signature absent from the visible-excitation data. The absence of such a signature indicates either that **QM** does not accumulate within the fs-TA time window or, more likely (*vide infra*), that its absorption overlaps strongly with the ESA of **1** in the probed spectral range (340–900 nm), precluding spectroscopic resolution of the two species.

### Simulated UV absorption spectra

To assess the applicability of the ADC(2)/def-SV(P) method, the calculated absorption spectrum of **1**+ was compared with experiments, showing reasonably good agreement (Fig. 4). In addition, vertical excitations, orbitals, and state assignments at different levels of theory (Tables S4–S7 and Fig. S18–S22) show qualitative agreement with the ADC(2)/aug-cc-PVDZ results.

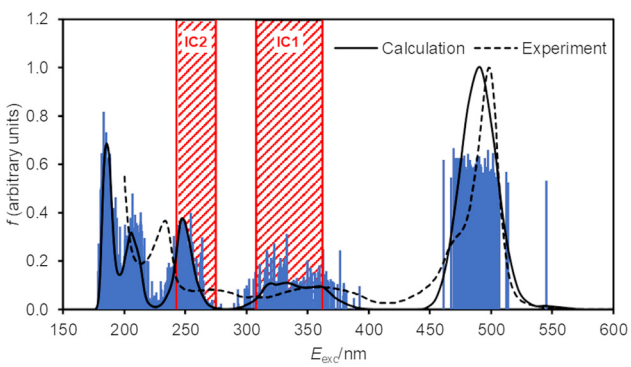



Fig. 4 Comparison of the ADC(2)/def-SV(P) absorption spectrum of **1**+ computed with COSMO ($H_2O$) solvation and the experimental spectrum (dashed black line) measured in $CH_3CN$–$H_2O$ (1 : 9). Excitation energies and oscillator strengths were computed by sampling initial conditions from a 10 ps long room temperature MD trajectory. Each of the $n$ = 20 transitions ($S_1 \rightarrow S_n$) was broadened with a Gaussian function of the same width (0.1 eV) (black line).

 This journal is © the Owner Societies 2026

We also note that for the isolated BODIPY chromophore, the ADC(2) method has been benchmarked against CASPT(12,11) calculations by De Vetta, González, and Corral.[52] The authors found that the ADC(2) results qualitatively reproduce the CASPT2 potential energy profiles away from the $S_1/S_0$ CI.

The absorption spectrum is characterized by four bands, slightly blue-shifted relative to the experiment. The first band, an intense absorption at 500 nm, corresponds to $S_1$ ($f = 0.586$), a locally excited state on the BODIPY moiety ($LE_{BP}$). The second band, broad and weak in the 300–400 nm region, comprises $S_2$, $S_3$ and $S_4$. $S_2$ and $S_3$ are also $LE_{BP}$ states ($f = 0.106$ and 0.049, respectively), while $S_4$ ($f = 0.087$) is a charge-transfer (CT) excitation from the phenyl to the BODIPY moiety ($CT_{PH\rightarrow BP}$). The third band, sharper and of medium intensity around 250 nm, contains $S_5$ through $S_8$. $S_5$, the lowest state of this band, has mixed $LE_{PH}$ + $CT_{PH\rightarrow BP}$ character; $S_6$ ($f = 0.191$) is dominated by $LE_{BP}$ with partial $CT_{BP\rightarrow PH}$ character; $S_7$ also shows mixed $CT_{PH\rightarrow BP}$ and $LE_{PH}$ character; and $S_8$ ($f = 0.154$) is a pure $CT_{BP\rightarrow}PH$ state. The band intensity is dominated by $S_6$ and $S_8$ at 4.98 and 5.14 eV. The mixed character of $S_5$ and $S_7$ (Table S4) implies that the relative $LE_{PH}$ and $CT_{PH\rightarrow}BP$ contributions in these states are likely geometry dependent – a point that becomes important in the dynamics simulations below. The fourth band is dominated by $S_{11}$ ($LE_{PH}$) at 6.01 eV and $S_{12}$ ($LE_{BP}$ with $CT_{BP\rightarrow}PH$ character) at 6.25 eV.

### Nonadiabatic dynamics simulations

To investigate the wavelength dependence of the photodynamics of $\mathbf{1}^+$, two sets of TSH simulations were carried out from distinct excitation-energy windows.

**Trajectory SH simulations from the 308–362 nm window (IC1).** The low energy window spanning 308–362 nm (3.42–4.02 eV), and denoted IC1 in Fig. 4, corresponds to excitations into the second absorption band of $\mathbf{1}^+$. Here, TSH simulations were initiated from three distinct adiabatic states $S_2$, $S_3$ and $S_4$ with fractional occupations of 0.32, 0.39, and 0.29, respectively. The time evolution of the average excited state populations is plotted in Fig. S34. One can see a very fast IC to the $S_1$ state, which becomes nearly completely populated in under 200 fs. A time constant of $\tau_e \approx 76$ fs was obtained by fitting the population rise to a monoexponential function (see computational methods and Fig. S35). The short rise time agrees with the fs-TA measurements (Fig. 3).

Deamination was not observed. In all trajectories started from IC1, with only a single exception, the system remained in the $S_1$ state until the end of the simulation time (1 ps). This confirms the presence of a minimum on the $S_1$ potential energy surface (PES) and the energy gap between the $S_1$ min and $S_0$ is sufficiently large to prevent internal conversion.

To simulate the fluorescence spectrum, we used geometries sampled from SH trajectories at 500 fs and at the end of the simulation (1000 fs). The ADC(2)/def-SV(P) vertical emission energies were convoluted using a Gaussian function with 0.1 eV width. Both spectra are centred between 500 and 610 nm, with a maximum around 538 nm, in good agreement with the measured fluorescence from the $S_1$ state at 500 nm upon excitation at 450 nm (Fig. 5).

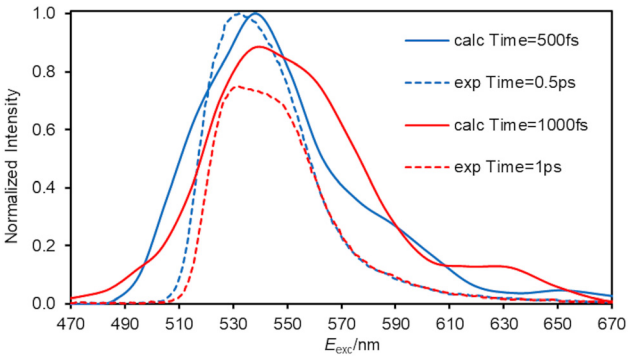



Fig. 5 Simulated fluorescence spectra from $S_1$ and $S_0$ energy differences in 500 fs (blue line) and 1000 fs (red line) from dynamics calculations started in energy window 308–362 nm (3.42–4.02 eV, IC1). Simple convolution with a Gaussian function of the width 0.1 eV was used. A comparison with measured spectra (dashed lines) is given as well.

The computed ESA spectrum of $\mathbf{1}^+$, shown in Fig. 6a, reveals that after 1 ps, excitations with significant oscillator strengths are grouped into two intense bands: one centred around 330 nm and the other between 450 and 590 nm, with the calculated maximum at 505 nm. Calculations performed at 250, 500, and 750 fs yielded similar spectra (Fig. S33), indicating that the system mostly reaches equilibrium in the $S_1$ state within 250 fs.

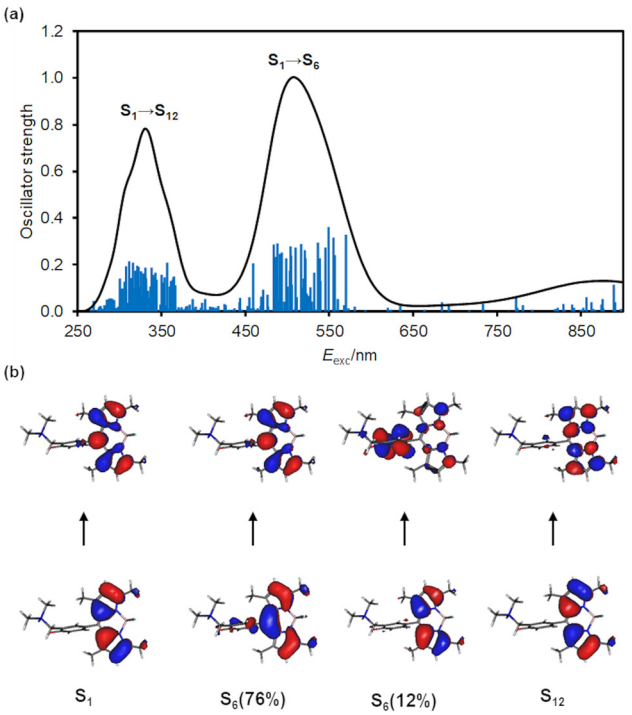



Fig. 6 (a) Computed ESA spectrum after 1 ps of simulation, initiated from the 308–362 nm (3.42–4.02 eV) energy window. Excitations from the current state up to $S_{20}$ are included (blue lines), with the convoluted ESA spectrum shown in black. (b) The dominant NTO pairs describing the states involved in excited to excited state transitions.

Analysis of the excited states contributing to the transitions with the highest oscillator strengths indicates that the intense band at 505 nm arises from transitions between $S_1$ and $S_6$ states, whereas the absorption around 330 nm originates from the $S_1 \rightarrow S_{12}$ transition. The dominant contribution to all these states is a local excitation on the BODIPY moiety of the $\mathbf{1}^+$ cation (Fig. 6b). Our calculations agree well with the experimental fs-TA spectrum in the 350 nm region (Fig. S39), showing an excited state absorption (ESA) band with the calculated maximum blue-shifted relative to experiments by approximately 20 nm. As for the second peak around 500 nm, here the GSB, SE and ESA signals overlap, precluding a direct comparison between the computed ESA signal and fs-TA measurements.

**Trajectory SH simulations from the 243–275 nm window (IC2).** TSH simulations initiated within the higher energy window in the 243–275 nm (4.50–5.10 eV) range, IC2, initially populate the adiabatic $S_5$–$S_8$ states. Compared to dynamics initiated at lower excitation energies, internal conversion to the $S_1$ state occurs more slowly (compare Fig. 7 and S34). In the higher energy regime, half of the population reaches the $S_1$ state only after ~200 fs, and a steady $S_1$ population is achieved only after ~700 fs (see Fig. 7). This delayed population of $S_1$ arises from trapping in the $S_5$ state which, at deformed geometries along the SH trajectories, has a dominant $CT_{PH\rightarrow BP}$ character (see Fig. 8c).

More specifically, the average population of $S_5$ increases from an initial 9% to approximately 65% within 40 fs and remains almost constant in the following 50 fs. The slow depopulation of $S_5$ begins at ~100 fs, and by the end of the simulation, only a few trajectories remain in the $S_5$ state. The decay times, $\tau_e$, obtained from exponential fitting (Fig. S36–S37) are very similar: 159 and 151 fs for the population of $S_1$ and depopulation of $S_5$, respectively. Because cooling *via* intermolecular vibrational energy transfer to the solvent is not possible in our simulations performed in implicit solvent, the trajectories retain excess vibrational energy after relaxing from higher states ($S_6$–$S_8$), possibly allowing them to surmount barriers and escape from the $S_5$ state. It is therefore reasonable to assume that, in solution, vibrational energy loss to the solvent could trap a larger fraction of the population in the $S_5$ state, which is the lowest electronic state in the third absorption band. The computed fluorescence spectrum along one of the trajectories trapped in the $S_5$ state (Fig. 8a) peaks at approximately 325 nm, in qualitative agreement with the observed weak fluorescence at 360 nm. This finding supports the assumption that population of the $S_5(CT_{PH\rightarrow BP})$ state is responsible for the observed anti-Kasha fluorescence. We should also note that the slower rise of the $S_1$ is in good agreement with our measurements, which indicate a delayed rise of the GSB and SE on a timescale of approximately 230 fs upon excitation at 250 nm (see Fig. 3 and corresponding text)

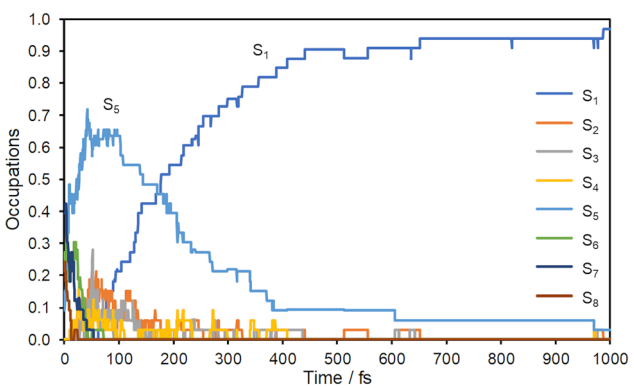



Fig. 7 The fraction of trajectories for each state as a function of time upon the excitation between 243 and 275 nm (4.5–5.1 eV).

Deamination, *i.e.*, cleavage of the C–N bond on the phenol moiety of $\mathbf{1}^+$, is observed in two trajectories. One of these trajectories is shown in Fig. 9. The initially populated state has $CT_{BP\rightarrow PH}$ electronic character. Within ~30 fs, it crosses several PESs and becomes stabilized as the adiabatic $S_2$ state. Fig. 9g shows that, as the state stabilizes, its electronic character remains unchanged. At the $S_3/S_2$ CI at 31 fs, the C–N distance is $d_{CN}$ = 1.52 Å and is further increased in the $S_2$ state (Fig. 9c, insets). This causes a steep rise in the potential energy of the $S_1$ state (locally excited on the BODIPY unit) and of the ground state. Consequently, the $S_2/S_1$ CI is reached at 97 fs, where the C–N distance has extended to 2.21 Å. The two nascent fragments retain their momentum, and the C–N distance continues to increase until the end of the simulation, where $d_{CN}$ reaches 8.44 Å. The average C–N bond lengths, considering only non-dissociative trajectories, are in the 1.4–1.8 Å range. In the two dissociative trajectories, the C–N distance leaves this range at around 60 fs. Thus, C–N dissociation occurs on an ultrafast timescale while the system is in the $CT_{BP\rightarrow PH}$ state. We should note, however, that the timescale of the deamination reaction may not be quantitatively accurate due to the limitations of the ADC(2) method in bond breaking regions with strong multiconfigurational character. Nevertheless, we believe that the results provide a reliable qualitative description of the underlying photochemical pathway.

In the 500–1000 fs time range, during which the $\mathbf{QMH}^+$ is formed, the energy gap between the $S_1$ and $S_0$ states is ~1.2 eV (1011 nm), and the oscillator strength of $S_1$ is ~0.01. Because these wavelengths are outside the range of our fs-TA and FlUC setups, spectroscopy could not provide direct evidence of whether the deamination reaction of **1** follows a Kasha or anti-Kasha pathway. Furthermore, the computed ESA of $\mathbf{1}(S_n)$ overlaps with the absorption of **QM** ($S_0$) (see Fig. S27, S39 and Table S11 in the SI), precluding time-resolution of their formation and decay.

## Discussion

Based on the combined experimental and theoretical results, we are now in a position to discuss several key aspects of the wavelength-dependent photodynamics of **1**. Upon visible excitation ($\lambda > 350$ nm), **1** exhibits an intense fluorescence band centred at 510 nm. In contrast, excitation in the UV region ($\lambda < 350$ nm) reveals qualitatively different behaviour (Fig. 2): in addition to the


This journal is © the Owner Societies 2026

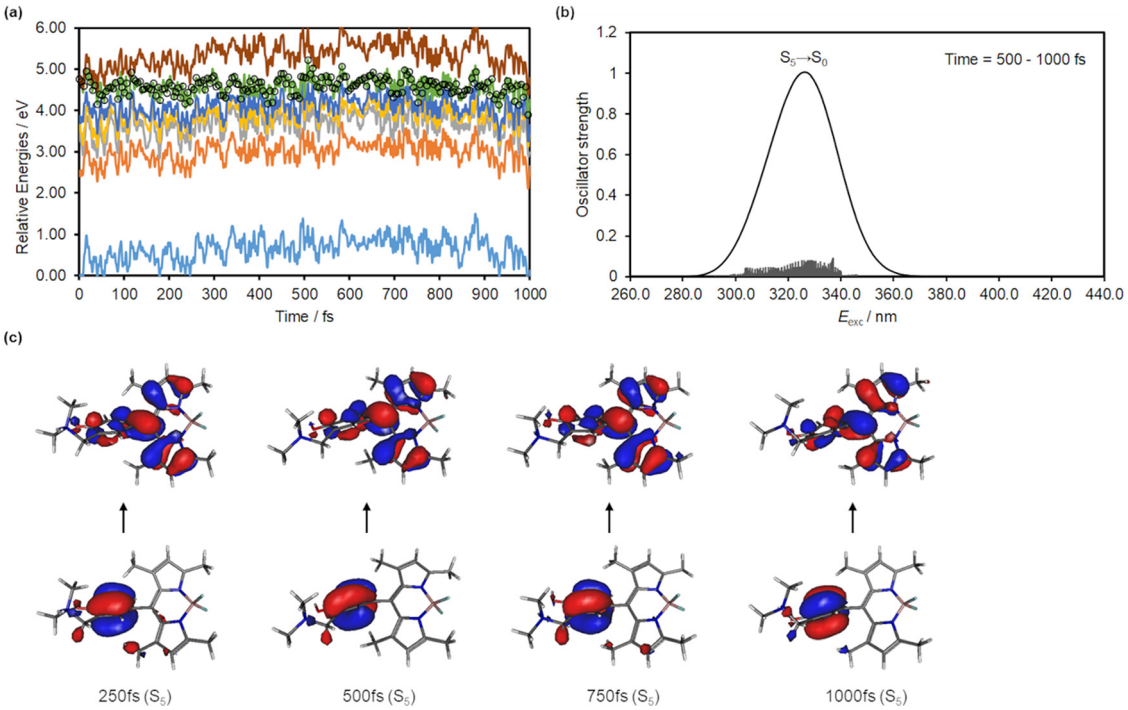



Fig. 8 (a) Time evolution of potential energies of the $S_0$ and excited states in the selected trajectory representing trapping of $\mathbf{1}^+$ in $S_5$. Black dots indicate the active state; (b) fluorescence spectrum computed from vertical emission energies and oscillator strengths in the 500–1000 fs time window for the selected trajectory. (c) Pairs of NTO orbitals for the current state ($S_5$: $CT_{PH \rightarrow BP}$) in selected times along the selected trajectory shown above.

dominant emission at 510 nm, a weaker high-energy fluorescence band appears in the 350–400 nm region. This feature indicates emission from higher-lying excited states and provides clear evidence of anti-Kasha photophysics.

Furthermore, UV excitation uniquely triggers photochemical reactivity, as deamination of **1** is observed only under these conditions.[20] Because the excited-state absorption signals of **1** and ground state absorption of **QM** overlap, the deamination time constant could not be determined from our transient absorption measurements.

These observations raise the question of whether emission and photochemistry originate from a common electronic state. Although emission from higher-lying excited states is intrinsically rare and our statistical sampling is therefore limited, nonadiabatic dynamics simulations identify the high-energy fluorescence as originating from the adiabatic $S_5$ state, characterized by CT from the phenyl group to the BODIPY moiety. Analysis of the $S_5$ character during the dynamics links it to either the $S_5$ or $S_7$ state at the FC geometry (these states are heavily mixed at the $S_0$ minimum geometry). We are inclined to suggest that, rather than representing a clear violation of Kasha's rule, this emission can be interpreted as an intraband manifestation of Kasha's rule. Specifically, $S_5$ corresponds to the lowest excited state within the third absorption band, and rapid internal conversion within this band ($\sim$40 fs, Fig. 7) is preserved. The emission from $S_5$ arises from the relatively large energy gap separating $S_5$ from $S_4$ (belonging to the second absorption band), which limits efficient interband internal conversion. Indeed, in our trajectories the $S_5$–$S_4$ gap is $\sim$0.5 eV and fluctuates between 0.2 and 0.8 eV. This enables partial population trapping in the $S_5$ state. TA measurements did not reveal the dynamics of higher excited states. This is because both the weak fluorescence and the higher excited-state absorption are masked by much stronger absorption from the first excited state of **1**. However, excited state absorption spectra match well with the calculated spectra, further validating the implemented theoretical model. In an attempt to detect the delayed rise of the stimulated emission signal in TA after excitation to higher excited states due to population trapping in the $S_5$ we were limited by a pronounced group velocity mismatch since the excitation and probe wavelength differ by nearly an octave.

An additional layer of complexity in **1** arises from the fact that the $S_5$ minimum lies $\sim$0.33 eV below its energy at the FC geometry and overlaps energetically with the second absorption band. This allows adiabatic population of the $S_5$ minimum upon excitation at 335 nm (see Fig. 2b and 4). Independently, TC-SPC reveals an excitation-wavelength dependence of the high-energy emission (Table S1) that is absent from the $S_1$ fluorescence, supporting distinct population pathways for the two emitters.

Experimentally, this picture is extended to longer times that cannot be reached by theoretical calculations. On picosecond timescales, for molecules excited to higher-lying excited states, global analysis of TA and FlUC spectra revealed dynamics characterized by surprisingly similar time constants, suggesting their common origin. While in high-energy fluorescence an initial blueshift was observed due to the slow intramolecular

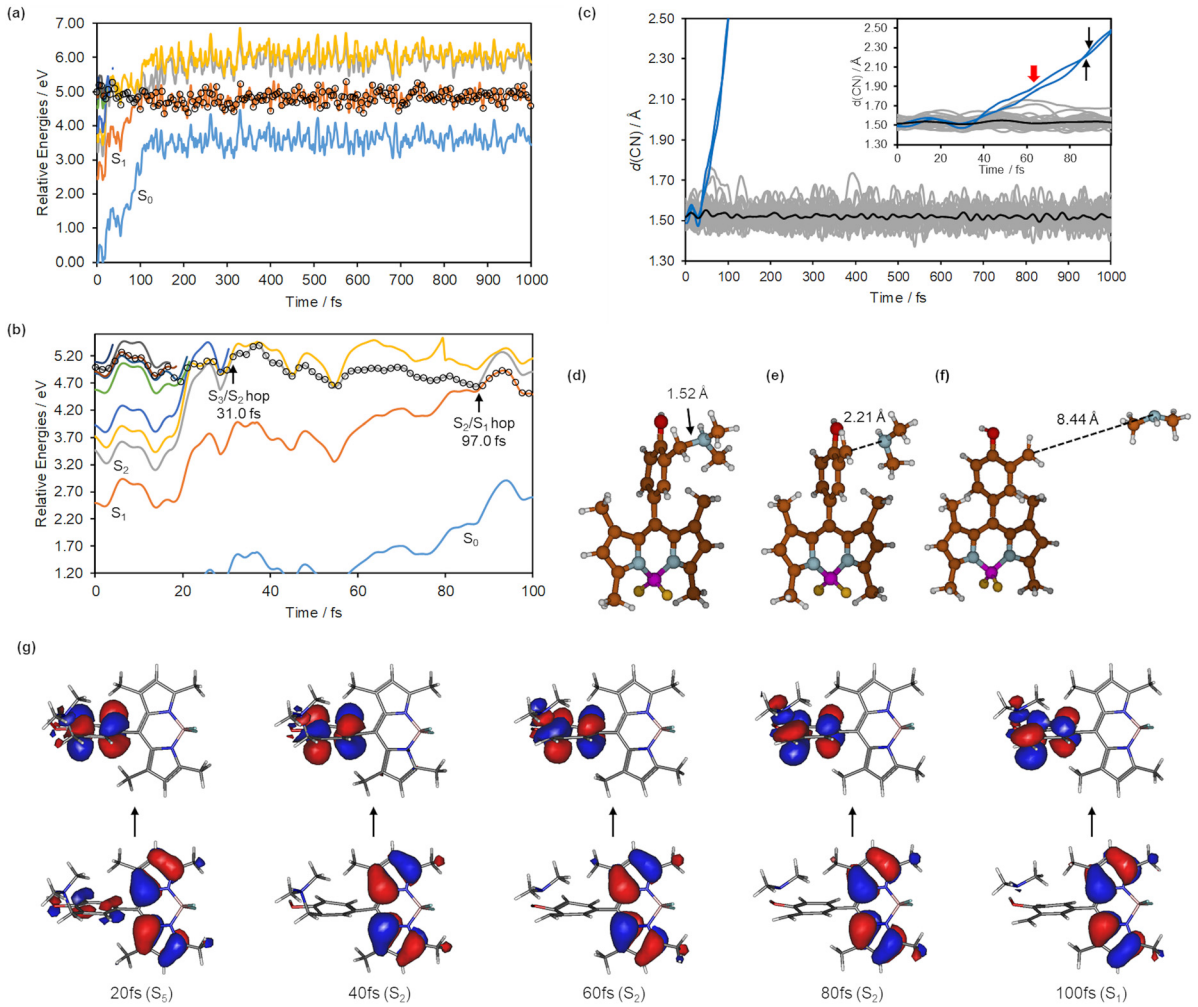



Fig. 9 (a) Time evolution of potential energies of the $S_0$ and excited states in the selected trajectory representing the C–N dissociation path. The black dots indicate the current state of the system in each time step. (b) Detailed view of the first 100 fs of the selected trajectory shown above. (c) Time evolution of the CN bond lengths in trajectories started from the higher energy window: blue – deamination process, gray – non dissociated, black – average non-dissociated. Black arrows indicate the $S_2/S_1$ hopping points. (d) Geometries of $\mathbf{1}^+$ in (d) in the $S_3/S_2$, (e) in the $S_2/S_1$ hopping point and (f) in the last point in the selected trajectory. (g) Pairs of NTO orbitals for the current state in selected times along the selected trajectory shown above.

rearrangements following the departure from the Frank–Condon region and thermalization with the solvent, transient absorption data suggest that fluorescence from the $S_1$ state is slightly redshifted within a few picoseconds due to the combined action of dynamic Stokes shift and vibrational cooling.

In contrast to high-energy fluorescence, photodeamination is associated with CT states of $CT_{BP\rightarrow PH}$ character. At the FC point, the lowest electronic states with partial $CT_{BP\rightarrow PH}$ character are the $S_6$ and $S_8$ (Table S4). TSH simulations started in the high-energy window confirm that these states play a key role in the deamination reaction. Our simulations also confirm that anti-Kasha photochemical processes are truly ultrafast.[12] The C–N bond scission occurs within 1.5 vibrational periods, much before intramolecular vibrational energy redistribution can take place. Although the energy of the $CT_{BP\rightarrow PH}$ state decreases as the C–N bond extends and crosses several excited states, it retains its character. Thus, the reaction proceeds on the diabatic $CT_{BP\rightarrow PH}$ state, even when this state becomes the adiabatic $S_1$ state. Interestingly, no experimental evidence for photodeamination from **1** was observed on ultra-fast time scales. Calculations indicate that the transient absorption signals of the photoproduct overlap strongly with those of **1**.

More generally, anti-Kasha photophysics and photochemistry are often discussed within a static framework, where slow internal conversion is attributed either to large energy gaps (poor Franck–Condon overlap) or weak electronic coupling.[12] From a dynamical perspective, these interpretations are closely related. According to the Hellmann–Feynman theorem, nonadiabatic couplings increase as electronic states approach each other and become infinite at degeneracies, *i.e.*, at a CI. Reduced access to CI (RACI)[53–55] can therefore lead to anti-Kasha behaviour. Of course, whether one describes the reaction in static or dynamical terms is largely a matter of personal preference and scientific perspective.[56]

 This journal is © the Owner Societies 2026

## Conclusions

The photodynamics of **1** is strongly wavelength dependent. Visible excitation leads to rapid internal conversion to the $S_1$ state, and results in green fluorescence without detectable photochemistry. In contrast, UV excitation opens additional pathways, giving rise to weak high-energy fluorescence and ultrafast deamination. The anomalous emission originates from the lowest electronic state of the third absorption band with phenyl-to-BODIPY CT character ($CT_{PH\rightarrow BP}$), where partial population trapping occurs due to suppression of internal conversion by the relatively large interband energy gap and restricted access to conical intersections. Therefore, this emission from a high-lying excited state is better viewed as an intraband extension rather than a strict violation of Kasha's rule. Our simulations show that photodeamination proceeds through higher CT states with BODIPY-to-phenyl character and involves rapid C–N bond cleavage occurring before intramolecular vibrational energy redistribution. Experimentally, we could not determine the deamination time constant because the excited-state absorption signal of **1** and ground state absorption of **QM 1** overlap. While the results highlight design principles for multichromophoric systems that enable control of photophysical and photochemical properties through selective wavelength excitation, they should be interpreted with caution. Photodeamination is a relatively rare event that is challenging to describe computationally. Furthermore, an accurate description of C–N bond cleavage requires multireference calculations. However, these effects could not be accurately treated within the framework of the present study due to computational and methodological limitations.

## Author contributions

M. S. developed the methodology and software. I. A. carried out the calculations, curated the data and prepared the visualizations. M. F., P. K., and V. B. performed the fs-TA experimental measurements. G. Z., P. D., A. C. and G. C. assisted in performing the experimental measurements. M. B. carried out the synthesis. N. D. contributed to data analysis and administered the project. S. V. supervised and directed the project and contributed to experimental measurements. I. A., S. V. and N. D. wrote the original draft of the manuscript, and contributed to review and discussion. All authors approved the final version of the manuscript.

## Conflicts of interest

There are no conflicts to declare.

## Data availability

The data supporting this article have been included as part of the supplementary information (SI). Supplementary information: further details of the experimental procedures, global analysis of FlUC and fs-TA data, theoretical characterization of the excited states (vertical and adiabatic excitation energies, oscillator strengths *etc.*), molecular orbitals, absorption simulations, ground state and excited state minima structures, description of the reaction coordinate for the deamination process in the ground and excited states, ground state dynamics, excited to excited state absorption simulations, and exponential fitting of the population in excited state dynamics and fluorescence spectra simulations. See DOI: https://doi.org/10.1039/d6cp02044e.

## Acknowledgements

This research was funded by the Croatian Science Foundation (grant. HRZZ-IP2022-10-4658). The research was sponsored in part by European Union's Horizon 2020 research and innovation programme under grant agreement no. 654148 Laserlab-Europe. This work was supported by the project Centre for Advanced Laser Techniques (CALT), co-funded by the European Union through the European Regional Development Fund under the Competitiveness and Cohesion Operational Programme (grant no. KK.01.1.1.05.0001). GZ, ND and SV are grateful to the Adris foundation for supporting this work. We are thankful for the allocation of the CPU time on the Supek and Isabela computing clusters at the Zagreb University Computing Center (SRCE) where most of the calculations were performed.

## Notes and references

1 M. Kasha, Characterization of Electronic Transitions in Complex Molecules, *Discuss. Faraday Soc.*, 1950, **9**, 14–19.
2 J. C. del Valle and J. Catalán, Kasha's rule: a reappraisal, *Phys. Chem. Chem. Phys.*, 2019, **21**, 10061–10069.
3 T. Itoh, Fluorescence and Phosphorescence from Higher Excited States of Organic Molecules, *Chem. Rev.*, 2012, **112**, 4541–4568.
4 M. Beer and H. C. Longuet-Higgins, Anomalous Light Emission of Azulene, *J. Chem. Phys.*, 1955, **23**, 1390–1391.
5 G. Viswanath and M. Kasha, Confirmation of the Anomalous Fluorescence of Azulene, *J. Chem. Phys.*, 1956, **24**, 574–577.
6 J. L. Kropp and C. C. Stanley, The temperature dependence of ovalene fluorescence, *Chem. Phys. Lett.*, 1971, **9**, 534–538.
7 A. Amirav, U. Even and J. Jortner, Intermediate level structure in the $S_2$ state of the isolated ultracold ovalene molecule, *Chem. Phys. Lett.*, 1980, **69**, 14–17.
8 M. Dantus and A. Zewail, Introduction: Femtochemistry, *Chem. Rev.*, 2004, **104**, 1717–1718.
9 T. Elsaesser, Introduction: Ultrafast Processes in Chemistry, *Chem. Rev.*, 2017, **117**, 10621–10622.
10 M. Maiuri, M. Garavelli and G. Cerullo, Ultrafast Spectroscopy: State of the Art and Open Challenges, *J. Am. Chem. Soc.*, 2020, **142**, 3–15.
11 P. Klán and J. Wirz, *Photochemistry of Organic Molecules*, Wiley, Chichester, 2009.

12 A. P. Demchenko, V. I. Tomin and P. T. Chou, Breaking the Kasha Rule for More Efficient Photochemistry, *Chem. Rev.*, 2017, **117**, 13353–13381.
13 T. Kumpulainen, B. Lang, A. Rosspeintner and E. Vauthey, Ultrafast Elementary Photochemical Processes of Organic Molecules in Liquid Solution, *Chem. Rev.*, 2017, **117**, 10826–10939.
14 J. Petersson, M. Eklund, J. Davidsson and L. Hammarström, Ultrafast Electron Transfer Dynamics of a Zn(II)porphyrin−Viologen Complex Revisited: $S_2$ *vs.* $S_1$ Reactions and Survival of Excess Excitation Energy, *J. Phys. Chem. B*, 2010, **114**, 14329–14338.
15 M. Andersson, J. Davidsson, L. Hammarström, J. Korppi-Tommola and T. Peltola, Photoinduced Electron Transfer Reactions in a Porphyrin-Viologen Complex: Observation of $S_2$ to $S_1$ Relaxation and Electron Transfer from the $S_2$ State, *J. Phys. Chem. B*, 1999, **103**, 3258–3262.
16 H.-W. Tseng, J.-Y. Shen, T.-Y. Kuo, T.-S. Tu, Y.-A. Chen, A. P. Demchenko and P.-T. Chou, Excited-state intramolecular proton-transfer reaction demonstrating anti-Kasha behaviour, *Chem. Sci.*, 2016, **7**, 655–665.
17 T. Piteša, M. Alešković, K. Becker, N. Basarić and N. Došlić, Photoelimination of Nitrogen from Diazoalkanes: Involvement of Higher Excited Singlet States in the Carbene Formation, *J. Am. Chem. Soc.*, 2020, **142**, 9718–9724.
18 M. Gazzetto, F. Artizzu, S. S. Attar, J. T. Casanova, L. Marchiò, L. Pilia, A. Monari, P. Deplano and A. Cannizzo, Beyond-Kasha Photochemistry in a Heteroleptic Platinum–Dithiolene Complex, *J. Am. Chem. Soc.*, 2026, **148**, 12186–12193.
19 M. Gazzetto, F. Artizzu, S. S. Attar, L. Marchiò, L. Pilia, E. J. Rohwer, T. Feurer, P. Deplano and A. Cannizzo, Anti-Kasha Conformational Photoisomerization of a Heteroleptic Dithiolene Metal Complex Revealed by Ultrafast Spectroscopy, *J. Phys. Chem. A*, 2020, **124**, 10687–10693.
20 K. Zlatić, I. Antol, L. Uzelac, A.-M. Mikecin Dražić, M. Kralj, C. Bohne and N. Basarić, Labeling of Proteins by BODIPY-Quinone Methides Utilizing Anti-Kasha Photochemistry, *ACS Appl. Mater. Interfaces*, 2020, **12**, 347–351.
21 K. Zlatić, M. Cindrić, I. Antol, L. Uzelac, B. Mihaljević, M. Kralj and N. Basarić, Wavelength dependent photochemistry of BODIPY–phenols and their applications in the fluorescent labeling of proteins, *Org. Biomol. Chem.*, 2021, **19**, 4891–4903.
22 K. Zlatić, M. Bogomolec, M. Cindrić, L. Uzelac and N. Basarić, Synthesis, photophysical properties, anti-Kasha photochemical reactivity and biological activity of vinyl- and alkynyl-BODIPY derivatives, *Tetrahedron*, 2022, **124**, 132995.
23 N. Basarić, M. Kralj, A.-M. Mikecin and M. Cindrić, *US Pat.*, US11103519B2, 2021, *Eur. Pat.*, EP3612538B1, 2021.
24 A. Loudet and K. Burgess, BODIPY Dyes and Their Derivatives: Syntheses and Spectroscopic Properties, *Chem. Rev.*, 2007, **107**, 4891–4932.
25 G. Ulrich, R. Ziessel and A. Harriman, The chemistry of fluorescent BODIPY dyes: versatility unsurpassed, *Angew. Chem., Int. Ed.*, 2008, **47**, 1184–1201.
26 N. Boens, B. Verbelen, M. J. Ortiz, L. Jiao and W. Dehaen, Synthesis of BODIPY dyes through postfunctionalization of the boron dipyrromethene core, *Coord. Chem. Rev.*, 2019, **399**, 213024.
27 I. S. Yadav and R. Misra, Design, synthesis and functionalization of BODIPY dyes: applications in dye-sensitized solar cells (DSSCs) and photodynamic therapy (PDT), *J. Mater. Chem. C*, 2023, **11**, 8688–8723.
28 N. Boens, V. Leen and W. Dehaen, Fluorescent indicators based on BODIPY, *Chem. Soc. Rev.*, 2012, **41**, 1130–1172.
29 T. Kowada, H. Maeda and K. Kikuchi, BODIPY-based probes for the fluorescence imaging of biomolecules in living cells, *Chem. Soc. Rev.*, 2015, **44**, 4953–4972.
30 A. Kamkaew, S. H. Lim, H. B. Lee, L. W. Kiew, L. Y. Chung and K. Burgess, BODIPY dyes in photodynamic therapy, *Chem. Soc. Rev.*, 2013, **42**, 77–88.
31 M. Gerecke, G. Bierhance, M. Gutmann, N. P. Ernsting and A. Rosspeintner, *Rev. Sci. Instrum.*, 2016, **87**, 053115.
32 P. Hamm, R. A. Kaindl and J. Stenger, *Opt. Lett.*, 2000, **25**, 1798–1800.
33 V. Brusar, M. Forjan, I. Ljubić, M. Alešković, K. Becker and S. Vdović, Ultrafast Photoelimination of Nitrogen from Upper Excited States of Diazoalkanes and the Fate of Carbenes Formed in the Reaction, *J. Org. Chem.*, 2023, **88**(7), 4286–4300.
34 L. L. E. Cigrang, *et al.*, Roadmap for Molecular Benchmarks in Nonadiabatic Dynamics, *J. Phys. Chem. A*, 2025, **129**(31), 7023–7050.
35 J. C. Tully, Molecular dynamics with electronic transitions, *J. Chem. Phys.*, 1990, **93**, 1061–1071.
36 J. Schirmer, Beyond the Random-Phase Approximation: A New Approximation Scheme for the Polarization Propagator, *Phys. Rev. A: At., Mol., Opt. Phys.*, 1982, **26**, 2395–2416.
37 A. B. Trofimov and J. Schirmer, An Efficient Polarization Propagator Approach to Valence Electron Excitation Spectra, *J. Phys. B: At., Mol. Opt. Phys.*, 1995, **28**, 2299–2324.
38 A. Dreuw and M. Wormit, The algebraic diagrammatic construction scheme for the polarization propagator for the calculation of excited states, *WIREs Comput. Mol. Sci.*, 2015, **5**, 82–95.
39 *TURBOMOLE V7.9 2024*, a development of University of Karlsruhe and Forschungszentrum Karlsruhe GmbH, 1989-2007, TURBOMOLE GmbH, since 2007, available from https://www.turbomole.org.
40 Y. J. Franzke, *et al.*, TURBOMOLE: Today and Tomorrow, *J. Chem. Theory Comput.*, 2023, **19**, 6859–6890.
41 C. Hättig and F. Weigend, CC2 excitation energy calculations on large molecules using the resolution of the identity approximation, *J. Chem. Phys.*, 2000, **113**, 5154–5161.
42 S. Hammes-Schiffer and J. C. Tully, Proton transfer in solution: Molecular dynamics with quantum transitions, *J. Chem. Phys.*, 1994, **101**, 4657–4667.
43 M. Sapunar, T. Piteša, D. Davidović and N. Došlić, Highly Efficient Algorithms for CIS Type Excited State Wave Function Overlaps, *J. Chem. Theory Comput.*, 2019, **15**, 3461–3469.

 This journal is © the Owner Societies 2026

44 A. Klamt, V. Jonas, T. Bürger and J. C. W. Lohrenz, Refinement and Parametrization of COSMO-RS, *J. Phys. Chem. A*, 1998, **102**, 5074–5085.
45 M. F. Gelin, Z. Lan, N. Došlić and W. Domcke, Computation of Time-Resolved Nonlinear Electronic Spectra From Classical Trajectories, *Wiley Interdiscip. Rev.:Comput. Mol. Sci.*, 2025, **15**, e70012.
46 I. Antol, Z. Glasovac, D. Margetić, R. Crespo-Otero and M. Barbatti, Insights on the Auxochromic Properties of the Guanidinium Group, *J. Phys. Chem. A*, 2016, **120**, 7088–7100.
47 *ZagHop, version 1.0*, 2026, available from https://github.com/marin-sapunar/ZagHop.
48 G. Schaftenaar and J. H. Noordik, Molden: a pre- and post-Processing Program for Molecular and Electronic Structures, *J. Comput.-Aided Mater. Des.*, 2000, **14**, 123–134.
49 A.-R. Allouche, Gabedit—A graphical user interface for computational chemistry softwares, *J. Comput. Chem.*, 2011, **32**, 174–182.
50 O. Braem, T. J. Penfold, A. Cannizzo and M. Chergui, A femtosecond fluorescence study of vibrational relaxation and cooling dynamics of UV dyes, *Phys. Chem. Chem. Phys.*, 2012, **14**, 3513–3519.
51 A. Cupane, M. Leone, E. Vitrano and L. Cordone, Low temperature optical absorption spectroscopy: an approach to the study of stereodynamic properties of hemeproteins, *Eur. Biophys. J.*, 1995, **23**, 385–398.
52 M. De Vetta, L. González and I. Corra, The Role of Electronic Triplet States and High-Lying Singlet States in the Deactivation Mechanism of the Parent BODIPY: An ADC(2) and CASPT2 Study, *ChemPhotoChem*, 2019, **3**, 727–738.
53 M. Mališ, Y. Loquais, E. Gloaguen, C. Jouvet, V. Brenner, M. Mons, I. Ljubić and N. Došlić, Non-radiative relaxation of UV photoexcited phenylalanine residues: probing the role of conical intersections by chemical substitution, *Phys. Chem. Chem. Phys.*, 2014, **16**, 2285–2288.
54 X.-L. Peng, S. Ruiz-Barragan, Z.-S. Li, Q.-S. Li and L. Blancafort, Restricted access to a conical intersection to explain aggregation induced emission in dimethyl tetraphenylsilole, *J. Mater. Chem. C*, 2016, **4**, 2802–2810.
55 R. Crespo-Otero, Q. Li and L. Blancafort, Exploring Potential Energy Surfaces for Aggregation-Induced Emission—From Solution to Crystal, *Chem. – Asian J.*, 2019, **14**, 700–714.
56 M. M. Nielsen, C. C. Wagen, L. A. Gomes, D. J. Tantillo, S. A. Lopez and E. N. Jacobsen, Ab Initio Molecular Dynamics Simulations for Organic Chemists—It is About Time!, *J. Am. Chem. Soc.*, 2026, **148**(16), 16549–16567.